GEOPHYSICS, VOL. 78, NO. 5 (SEPTEMBER-OCTOBER 2013); P. U65–U76, 17 FIGS.
10.1190/GEO2012-0278.1

Downloaded 11/16/13 to 138.67.128.104. Redistribution subject to SEG license or copyright; see Terms of Use at http://library.seg.org/

Illumination compensation for image-domain wavefield tomography

Tongning Yang[1], Jeffrey Shragge[2], and Paul Sava[3]

ABSTRACT

Image-domain wavefield tomography is a velocity model building technique using seismic images as the input and seismic wavefields as the information carrier. However, the method suffers from the uneven illumination problem when it applies a penalty operator to highlighting image inaccuracies due to the velocity model error. The uneven illumination caused by complex geology such as salt or by incomplete data creates defocusing in common-image gathers even when the migration velocity model is correct. This additional defocusing violates the wavefield tomography assumption stating that the migrated images are perfectly focused in the case of the correct model. Therefore, defocusing rising from illumination mixes with defocusing rising from the model errors and degrades the model reconstruction. We addressed this problem by incorporating the illumination effects into the penalty operator such that only the defocusing by model errors was used for model construction. This was done by first characterizing the illumination defocusing in gathers by illumination analysis. Then an illumination-based penalty was constructed that does not penalize the illumination defocusing. This method improved the robustness and effectiveness of image-domain wavefield tomography applied in areas characterized by poor illumination. Our tests on synthetic examples demonstrated that velocity models were more accurately reconstructed by our method using the illumination compensation, leading to a more accurate model and better subsurface images than those in the conventional approach without illumination compensation.

INTRODUCTION

Building an accurate and reliable velocity model remains one of the biggest challenges in current seismic imaging practice. In regions characterized by complex subsurface structure, prestack wave-equation depth migration (e.g., one-way wave-equation migration or reverse-time migration) is a powerful tool for accurately imaging the earth's interior (Gray et al., 2001; Etgen et al., 2009). The widespread use of these advanced imaging techniques drives the need for high-quality velocity models because these migration methods are very sensitive to model errors (Symes, 2008b; Woodward et al., 2008; Virieux and Operto, 2009).

Wavefield tomography represents a family of techniques for velocity model building using seismic wavefields (Tarantola, 1984; Woodward, 1992; Pratt, 1999; Sirgue and Pratt, 2004; Plessix, 2006; Vigh and Starr, 2008; Plessix, 2009). The core of wavefield tomography is using a wave equation (typically constant density acoustic) to simulate wavefields as the information carrier. Wavefield tomography is usually implemented in the data domain by adjusting the velocity model such that simulated and recorded data match (Tarantola, 1984; Pratt, 1999). This match is based on the strong assumption that the wave equation used for simulation is consistent with the physics of the earth. However, this is unlikely to be the case when the earth is characterized by strong (poro)elasticity. Significant effort is often directed toward removing the components of the recorded data that are inconsistent with the assumptions used.

Wavefield tomography can also be implemented in the image domain rather than in the data domain. Instead of minimizing the data misfit, the techniques in this category update the velocity model by optimizing quality of the image, which is the crosscorrelation of wavefields extrapolated from the source and receivers. Such techniques are also known as wave-equation migration velocity analysis (Sava and Biondi, 2004a, 2004b). For such methods, the image quality is optimized when the data are migrated with the correct velocity model, as stated by the semblance principle (Al-Yahya,

Manuscript received by the Editor 18 July 2012; revised manuscript received 8 April 2013; published online 8 August 2013.
[1]Formerly Colorado School of Mines, Center for Wave Phenomena, Golden, Colorado, USA; presently BP America, Houston, Texas, USA. E-mail: tongning.yang@bp.com.
[2]University of Western Australia, School of Earth and Environment, Perth, Australia. E-mail: jshragge@gmail.com.
[3]Colorado School of Mines, Center for Wave Phenomena, Golden, Colorado, USA. E-mail: psava@mines.edu.
© 2013 Society of Exploration Geophysicists. All rights reserved.

Downloaded 11/16/13 to 138.67.128.104. Redistribution subject to SEG license or copyright; see Terms of Use at http://library.seg.org/

1989). The common idea is to optimize the coherency of reflection events in common-image gathers (CIGs) via velocity model updating (Stork, 1992). Because images are obtained using full seismograms, and velocity estimation also uses seismic wavefields as the information carrier, these techniques can be regarded as a particular type of wavefield tomography, and we refer to them as image-domain wavefield tomography. The terminology highlights the fact that the methods belong to the wavefield tomography family. Unlike traditional ray-based reflection tomography methods, image-domain wavefield tomography uses band-limited wavefields in the optimization procedure. Using the wavefield as the information carrier allows the technique to characterize complicated wave propagation phenomena such as multipathing in the subsurface (Zhang and Schuster, 2010). In addition, the band-limited characteristics of the wave-equation engine accurately approximates wave propagation in the subsurface and produces more reliable velocity updates than those obtained by ray-based tomography methods.

Differential semblance optimization (DSO) is one implementation of image-domain wavefield tomography. The essence of the method is to minimize the difference of the same reflection between neighboring offsets or angles. Symes and Carazzone (1991) propose a criterion for measuring coherency from offset gathers and establish the theoretic foundation for DSO. The concept is then generalized to space-lag (subsurface-offset) and angle-domain gathers (Shen and Calandra, 2005; Shen and Symes, 2008). Space-lag gathers (Rickett and Sava, 2002; Shen and Calandra, 2005) and angle-domain gathers (Sava and Fomel, 2003; Biondi and Symes, 2004) are two popular choices among various types of gathers used for velocity analysis. These gathers are obtained by wave-equation migration and are free of artifacts usually found in conventional offset gathers obtained by Kirchhoff migration. Thus, they are suitable for applications in complex earth models (Stolk and Symes, 2004).

DSO implemented using horizontal space-lag gathers constructs a penalty operator which annihilates the energy at zero lag and enhances the energy at nonzero lags (Shen et al., 2003). This construction assumes that migrated images are perfectly focused at zero lag when the model is correct. If the model is incorrect, reflections in the gathers are defocused and the reflection energy spreads to nonzero lags. As a result, any energy left after applying the penalty is attributed to the result of model errors. However, this assumption is violated in practice when the subsurface illumination is uneven. Uneven illumination introduces additional defocusing such that images are not perfectly focused even if the velocity is correct, and it usually results from incomplete surface recorded data or from complex subsurface structure. Nemeth et al. (1999) show that the least-squares migration method can compensate the poor image quality due to the data deficiency. This method, however, is costly because it requires many iterations to converge (Shen et al., 2011). In complex subsurface regions, such as subsalt, uneven illumination is a general problem, and it deteriorates the quality of imaging and velocity model building (Leveille et al., 2011). Leveille et al. (2011) and Shen et al. (2011) show that the quality of migrated images can be optimized by illumination-based weighting generated from a demigration/remigration procedure. Tang and Biondi (2011) compute the diagonal of the Hessian matrix for the migration operator and use it for illumination compensation of the image before velocity analysis. These approaches effectively improve the quality of subsurface images, especially the balance of the amplitude. Nonetheless, they do not investigate the negative impact of illumination on the velocity model building. Furthermore, the misleading velocity updates due to uneven illumination remain an unsolved problem.

In this paper, we address the problem of uneven illumination associated with image-domain wavefield tomography. We first separate the illumination effects from velocity error effect on the space-lag gathers used for DSO. The idea is to construct an "impulse" image (a synthetic reflectivity model) that contains uniform point scatterers at the locations of horizons picked from current migrated image. The impulse response in space-lag gathers is computed by applying demigration/migration with the current estimated model and acquisition geometry. The result captures the defocusing due to illumination effects in the gathers. The reciprocal of the new gathers provides the weights (i.e., an illumination-based penalty operator) in the objective function. For good subsurface illumination, energy focus only around zero lag in the new gathers. In this case, the weights (new penalty) is equivalent to the conventional DSO penalty, and the corresponding objective function reduces to the standard DSO objective function. In the following sections, we first review the objective function and gradient computation for image-domain wavefield tomography. Next, we explain how the uneven illumination degrades wavefield tomography and we propose the illumination-based penalty as the solution. The construction of the new penalty and corresponding gradient calculation are also explained in detail. We illustrate our method with two synthetic examples representing two different types of illumination problems. The success of the approach is confirmed by the improvements of the results obtained by our method compared with those obtained by the conventional method.

THEORY

For clarity, we organize the theory section into three subsections. In the first part, we explain how to compute the gradient for conventional DSO using the adjoint-state method. Readers who are familiar with the computation can safely skip it. In the second part, we analyze how the illumination affects gather focusing by examining the formula for stacking the gathers. We then derive our formulation for the new penalty operator, which compensates the illumination effects. In the last part, we illustrate the gradient computation given the new penalty operator.

Gradient computation for DSO

In image-domain wavefield tomography using horizontal space-lag extended images (subsurface-offset CIGs), the objective function is formulated by applying the idea of DSO and the gradient is computed using the adjoint-state method (Plessix, 2006). More details and advantages of using the adjoint-state method for gradient computation can be also found in Plessix (2006). For simplicity, we show the computation in the frequency domain rather than in the time domain. The first step of the adjoint-state method is defining the state variables, through which the objective function is related to the model parameter. The state variables for our problem are the source and receiver wavefields u_s and u_r obtained by solving the following acoustic wave equation:

Downloaded 11/16/13 to 138.67.128.104. Redistribution subject to SEG license or copyright; see Terms of Use at http://library.seg.org/

$$\begin{bmatrix} \mathcal{L}(\mathbf{x},\omega,m) & 0 \\ 0 & \mathcal{L}^*(\mathbf{x},\omega,m) \end{bmatrix} \begin{bmatrix} u_s(j,\mathbf{x},\omega) \\ u_r(j,\mathbf{x},\omega) \end{bmatrix} = \begin{bmatrix} f_s(j,\mathbf{x},\omega) \\ f_r(j,\mathbf{x},\omega) \end{bmatrix}, \quad (1)$$

where f_s is a point or plane source, f_r are the record data, $j = 1, 2, \ldots, N_s$; where N_s is the number of shots, ω is the angular frequency, and $\mathbf{x}$ are the space coordinates $\{x, y, z\}$. The wave operator $\mathcal{L}$ and its adjoint $\mathcal{L}^*$ propagate the wavefields forward and backward in time, respectively, using a two-way wave equation. Thus, $\mathcal{L}$ is formulated as

$$\mathcal{L} = -\omega^2 m - \Delta, \quad (2)$$

where Δ is the Laplace operator and m represents the model (slowness squared). Such a formulation treats the wavefields as unknown vectors in the linear system of equation 1, and we can obtain the solution by solving the system of linear equations. A similar representation can also be found in Pratt (1999).

In the second step of the adjoint-state method, first the objective function is formulated. Then, the adjoint sources are derived from the objective function. The adjoint sources are used to compute the adjoint-state variables required by the gradient computation. The objective function for image-domain wavefield tomography measures the image incoherency caused by the model errors. Therefore, the inversion simultaneously reconstructs the model and improves the image quality by minimizing the objective function.

The DSO objective function based on space-lag CIGs is

$$\mathcal{H}_{\boldsymbol{\lambda}} = \frac{1}{2} \| P(\boldsymbol{\lambda}) r(\mathbf{x}, \boldsymbol{\lambda}) \|^2_{\mathbf{x},\boldsymbol{\lambda}}, \quad (3)$$

where r is the extended image defined as

$$\begin{aligned} r(\mathbf{x},\boldsymbol{\lambda}) &= \sum_j \sum_\omega \overline{u_s(j,\mathbf{x}-\boldsymbol{\lambda},\omega)}\, u_r(j,\mathbf{x}+\boldsymbol{\lambda},\omega) \\ &= \sum_j \sum_\omega T(-\boldsymbol{\lambda}) \overline{u_s(j,\mathbf{x},\omega)} T(\boldsymbol{\lambda}) u_r(j,\mathbf{x},\omega). \end{aligned} \quad (4)$$

The overline represents complex conjugate. In this article, we consider the space lags in the horizontal directions only, i.e., $\boldsymbol{\lambda} = \{\lambda_x, \lambda_y, 0\}$.

The operator T represents the space shift applied to the wavefields and is defined by

$$T(\boldsymbol{\lambda}) u(j,\mathbf{x},\omega) = u(j,\mathbf{x}+\boldsymbol{\lambda},\omega). \quad (5)$$

The penalty operator $P(\boldsymbol{\lambda})$ annihilates the focused energy at zero lag and highlights the energy of residual moveout at nonzero lag (Shen and Symes, 2008):

$$P(\boldsymbol{\lambda}) = |\boldsymbol{\lambda}|. \quad (6)$$

Our contribution consists of replacing this operator with a new illumination-based penalty operator, as it will be explained in the following subsection. The objective function $\mathcal{H}_{\boldsymbol{\lambda}}$ is minimized when the reflections focus at zero lag, which is an indication of the correct velocity model.

The adjoint sources g_s and g_r are computed as the derivatives of the objective function $\mathcal{H}_{\boldsymbol{\lambda}}$ shown in equation 3 with respect to the state variables u_s and u_r:

$$\begin{aligned} \begin{bmatrix} g_s(j,\mathbf{x},\omega) \\ g_r(j,\mathbf{x},\omega) \end{bmatrix} &= \begin{bmatrix} \frac{\partial \mathcal{H}_{\boldsymbol{\lambda}}}{\partial u_s} \\ \frac{\partial \mathcal{H}_{\boldsymbol{\lambda}}}{\partial u_r} \end{bmatrix} \\ &= \begin{bmatrix} \sum_{\boldsymbol{\lambda}} T(\boldsymbol{\lambda}) P(\boldsymbol{\lambda}) \overline{P(\boldsymbol{\lambda}) r(\mathbf{x},\boldsymbol{\lambda})} T(\boldsymbol{\lambda}) u_r(j,\mathbf{x},\omega) \\ \sum_{\boldsymbol{\lambda}} T(-\boldsymbol{\lambda}) P(\boldsymbol{\lambda}) \overline{P(\boldsymbol{\lambda})} r(\mathbf{x},\boldsymbol{\lambda}) T(-\boldsymbol{\lambda}) u_s(j,\mathbf{x},\omega) \end{bmatrix}. \end{aligned} \quad (7)$$

The adjoint state variables a_s and a_r are the wavefields obtained by backward and forward modeling, respectively, using the corresponding adjoint sources defined in equation 7:

$$\begin{bmatrix} \mathcal{L}^*(\mathbf{x},\omega,m) & 0 \\ 0 & \mathcal{L}(\mathbf{x},\omega,m) \end{bmatrix} \begin{bmatrix} a_s(j,\mathbf{x},\omega) \\ a_r(j,\mathbf{x},\omega) \end{bmatrix} = \begin{bmatrix} g_s(j,\mathbf{x},\omega) \\ g_r(j,\mathbf{x},\omega) \end{bmatrix}, \quad (8)$$

where $\mathcal{L}$ and $\mathcal{L}^*$ are the same wave propagation operators used in equation 1.

The last step of the gradient computation is the correlation between state variables and adjoint state variables:

$$\begin{aligned} \frac{\partial \mathcal{H}_{\boldsymbol{\lambda}}}{\partial m} = \sum_j \sum_\omega \frac{\partial \mathcal{L}}{\partial m} \big(& u_s(j,\mathbf{x},\omega) \overline{a_s(j,\mathbf{x},\omega)} \\ & + u_r(j,\mathbf{x},\omega) \overline{a_r(j,\mathbf{x},\omega)} \big), \end{aligned} \quad (9)$$

where $\partial\mathcal{L}/\partial m$ is the partial derivative of the wave propagation operator with respect to the model parameter. Using the definition of $\mathcal{L}$ in equation 2, it is apparent that $\partial L/\partial m = -\omega^2$. From equation 9, one may notice that the gradient for image-domain wavefield tomography consists of two correlations because the source and receiver wavefields are defined as the state variables.

The derivation above shows the construction of the image-domain wavefield tomography objective function and its gradient. Given these two components, the solution to the inverse problem is found by minimizing the objective function using nonlinear gradient-based iterative methods (Knyazev and Lashuk, 2007). In each iteration, the gradient is computed and the model update is calculated by a line search in the steepest descent or conjugate gradient directions.

Construction of illumination-based penalty

Conventional DSO penalizes defocusing that results from velocity errors in the space-lag gathers. However, defocusing can also be generated due to uneven illumination. In general, these two kinds of defocusing are indistinguishable to the velocity analysis procedure. The penalty operator in equation 6 emphasizes all energy away from zero lag and includes the defocusing caused by the velocity error and by the uneven illumination. Thus, the standard DSO penalty leads to a residual that is much larger than what would be expected for a given error in the model. Penalizing the defocusing due to the

Downloaded 11/16/13 to 138.67.128.104. Redistribution subject to SEG license or copyright; see Terms of Use at http://library.seg.org/

illumination misleads the inversion and results in overcorrection and artificial updates.

To analyze the illumination effects on focusing and construct the illumination-based penalty, we first illustrate the focusing mechanism for reflections in space-lag gathers. Yang and Sava (2010) derive the analytic formula for the reflection moveout in the extended images. Assuming constant local velocity, a reflection in space-lag gathers obtained by migrating one shot experiment is a straight line in 2D and a plane in 3D:

$$z(\boldsymbol{\lambda}) = d_0 - \frac{\tan\theta(\mathbf{q}\cdot\boldsymbol{\lambda})}{n_z}. \tag{10}$$

Here, d_0 represents the depth of the reflection corresponding to the chosen CIG location, $\boldsymbol{\lambda}$ represents the horizontal space lag $\boldsymbol{\lambda} = \{\lambda_x, \lambda_y, 0\}$, n_z is the vertical component of the unit vector normal to the reflection plane, $\mathbf{q}$ is the unit vector, and θ is the reflection angle.

When we stack the gathers obtained with a correct model from all available shots, the straight lines or planes corresponding to reflections from different shots are superimposed and interfere to form a focused point at zero lag (Yang and Sava, 2010). Good interference of such events, however, occurs only if the reflector point is well illuminated by the experiments. In other words, the surface shot coverage must be large enough and regularly distributed. Also, the subsurface illumination must be even so that the reflector is illuminated on a sufficient range of reflection angles from the surface. If either of these conditions is not satisfied, the reflection energy does not interfere perfectly and the gathers defocus, even if the correct model is used for the imaging.

To alleviate the negative influence of uneven illumination, we need to include the illumination information in the tomographic procedure. One approach uses the illumination information as a weighting function to preconditioning the gathers. The gathers in poor illumination areas are downweighted because the defocusing information is less reliable than the gathers in good illumination areas. This approach stabilizes the inversion but decreases the accuracy of the results because the useful velocity information in poor illumination areas is ignored. The poor illumination area, however, is exactly the place where we want to make use of all available information for the model building. To overcome the illumination problem and preserve the useful information in the tomography, we introduce a new illumination-based penalty operator to replace the conventional DSO penalty operator. The new operator is constructed such that it only emphasizes the defocusing caused by the velocity error and ignores the defocusing caused by uneven illumination. To achieve this goal, we analyze the image defocusing due to uneven illumination by applying illumination analysis.

Illumination analysis in the framework of wave-equation migration is formulated using the solution to migration deconvolution problems (Berkhout, 1982; Yu and Schuster, 2003; Xie et al., 2006; Mao et al., 2010). Migration deconvolution first establishes a linear relationship between a reflectivity distribution $\tilde{r}$ and seismic data d:

$$\mathcal{M}\tilde{r}(\mathbf{x}) = d, \tag{11}$$

where $\mathcal{M}$ represents a forward Born modeling operator that is linear with respect to the reflectivity. A migrated image is obtained by applying the adjoint of the modeling operator $\mathcal{M}^*$ to the data,

$$\mathcal{M}^* d = \mathcal{M}^*\mathcal{M}\tilde{r}(\mathbf{x}) = r(\mathbf{x}), \tag{12}$$

where r is a migrated image. Here, no extended images are involved yet. Note that the migrated image is the result of blurring the reflectivity $\tilde{r}$ by $\mathcal{M}^*\mathcal{M}$, which is the Gauss-Newton approximation to the Hessian of the least-squares misfit function, or alternatively, the Hessian of the Born approximation (linearized) inverse problem. In either case, operator $\mathcal{M}^*\mathcal{M}$ represents the second derivative of the least-squares misfit function with respect to the image by

$$\tilde{r}(\mathbf{x}) = (\mathcal{M}^*\mathcal{M})^{-1} r(\mathbf{x}), \tag{13}$$

where $(\mathcal{M}^*\mathcal{M})^{-1}$ includes the subsurface illumination information associated with the velocity structure and acquisition geometry. In practice, the matrix $(\mathcal{M}^*\mathcal{M})^{-1}$ is effectively noninvertible due to the realistic acquisition geometry, but we can evaluate its impact by applying a cascade of demigration and migration $\mathcal{M}^*\mathcal{M}$ to an image:

$$r_e(\mathbf{x}) = \mathcal{M}^*\mathcal{M} r(\mathbf{x}). \tag{14}$$

The quotient $r_e(\mathbf{x})/r(\mathbf{x})$ approximates the diagonal elements of the Hessian and characterizes the illumination effects (Symes, 2008a). One application of such analysis is to construct weights for illumination compensation of migrated image (Guitton, 2004; Gherasim et al., 2010; Tang and Biondi, 2011). Equation 14 only computes the illumination effects distributed at image points. In our problem, we are concerned with the defocusing caused by the illumination in the space-lag gathers, and we need to evaluate the illumination effects at image points and along their space-lag extension. To achieve this, we can generalize equation 14 to the extended image space $\mathbf{x} - \boldsymbol{\lambda}$:

$$r_e(\mathbf{x}, \boldsymbol{\lambda}) = \mathcal{M}^*\mathcal{M} r'(\mathbf{x}), \tag{15}$$

where $r'(\mathbf{x})$ is the reference image and $r_e(\mathbf{x}, \boldsymbol{\lambda})$ are the output illumination gathers containing defocusing associated with illumination effects. Notice that we use the same symbol $\mathcal{M}^*$ to represent the imaging operator in equations 14 and 15. Nonetheless, $\mathcal{M}^*$ in equation 14 applies the regular imaging condition and outputs $r_e(\mathbf{x})$, whereas $\mathcal{M}^*$ in equation 15 applies the extended imaging condition and output $r_e(\mathbf{x}, \boldsymbol{\lambda})$. The defocusing in the illumination gathers is the consequence of uneven illumination and should not be penalized by the penalty operator in the velocity updating process.

The implementation of equation 15 consists of several steps. We first pick all horizons from the current migrated image, and then we insert uniform-amplitude point scatterers at the positions of these picked horizons to obtain the reference image $r'(\mathbf{x})$. Next, we use the current estimated velocity model to run Born modeling operator $\mathcal{M}$ given $r'(\mathbf{x})$ as the reflectivity model. After we generate the data, we migrate the data using the imaging operator $\mathcal{M}^*$ to obtain illumination gathers $r_e(\mathbf{x}, \boldsymbol{\lambda})$. During the process, we use the same velocity model (current estimated one) in the modeling and migration. This is equivalent to migrating the data using the true model. The resulting gathers should be perfectly focused. If not, the defocusing can only be attributed to acquisition or illumination. Therefore, applying equation 15 characterizes the

Downloaded 11/16/13 to 138.67.128.104. Redistribution subject to SEG license or copyright; see Terms of Use at http://library.seg.org/

defocusing due to illumination effects in space-lag gathers given the current acquisition and current estimated model. In other words, reference image $r'(\mathbf{x})$ acts like an impulse, and illumination gathers $r_e(\mathbf{x}, \boldsymbol{\lambda})$ contain the impulse response for the acquisition system and subsurface structure in the extended image space. Given the illumination gathers, we are able to isolate the defocusing due to illumination using a new penalty in the inversion. Thus, we can construct the illumination-based penalty operator as

$$P_e(\mathbf{x}, \boldsymbol{\lambda}) = \frac{1}{|r_e(\mathbf{x}, \boldsymbol{\lambda})| + \epsilon}, \tag{16}$$

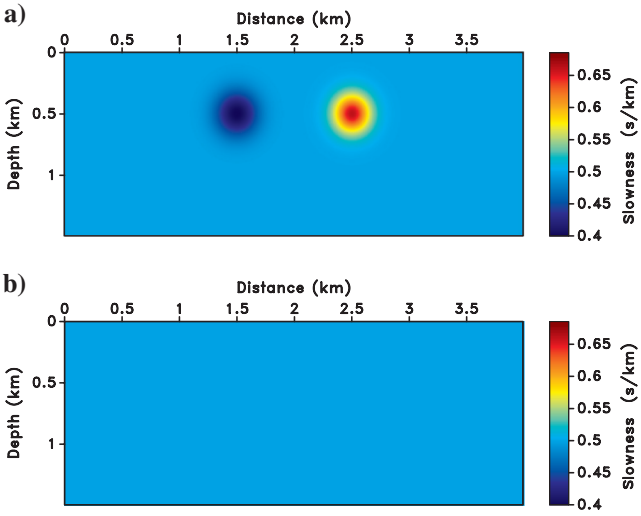


Figure 1. (a) The true model used to generate the data and (b) the initial constant model for inversion.

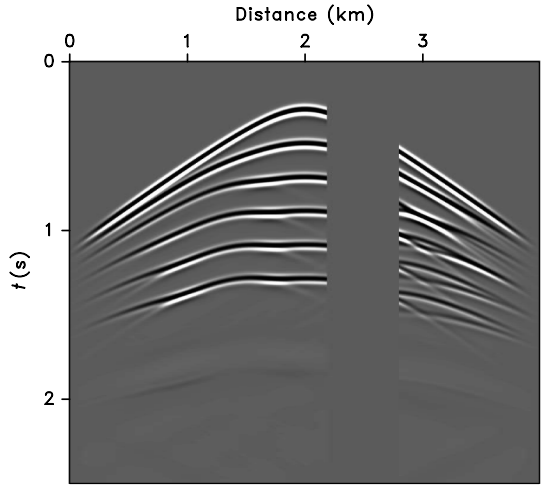


Figure 2. The shot gathers at 2.0 km with direct arrival muted showing a gap of 0.6 km in the acquisition surface. The gap simulates an obstacle that prevents data acquisition, e.g., a drilling platform.

where ϵ is a damping factor used to stabilize the division. By definition, this penalty operator has low values in the area of defocusing due to uneven illumination and high values in the rest. Thus, this operator is consistent with our idea of avoiding penalty to reflection energy irrelevant to velocity errors, e.g., the artifacts caused by illumination. Replacing the conventional penalty in equation 6 with the one in equation 16 is the basis for our illumination compensated image-domain wavefield tomography. Note that the DSO penalty operator is a special case of our new penalty operator and corresponds to the case of perfect subsurface illumination and wide-band data.

Gradient computation with illumination-based penalty

Using the new penalty operator $P_e(\mathbf{x}, \boldsymbol{\lambda})$ defined in equation 16, we can formulate the objective function for illumination-compensated wavefield tomography as

$$\mathcal{H}'_{\boldsymbol{\lambda}} = \frac{1}{2}\|P_e(\mathbf{x}, \boldsymbol{\lambda}) r(\mathbf{x}, \boldsymbol{\lambda})\|^2_{\mathbf{x},\boldsymbol{\lambda}}. \tag{17}$$

The gradient computation for the new objective function can also be done using the adjoint-state method. One difference, however, is that the penalty operator P_e is model-dependent in the new formulation. Thus, we need to take this into account when we compute the adjoint sources, which can be computed as

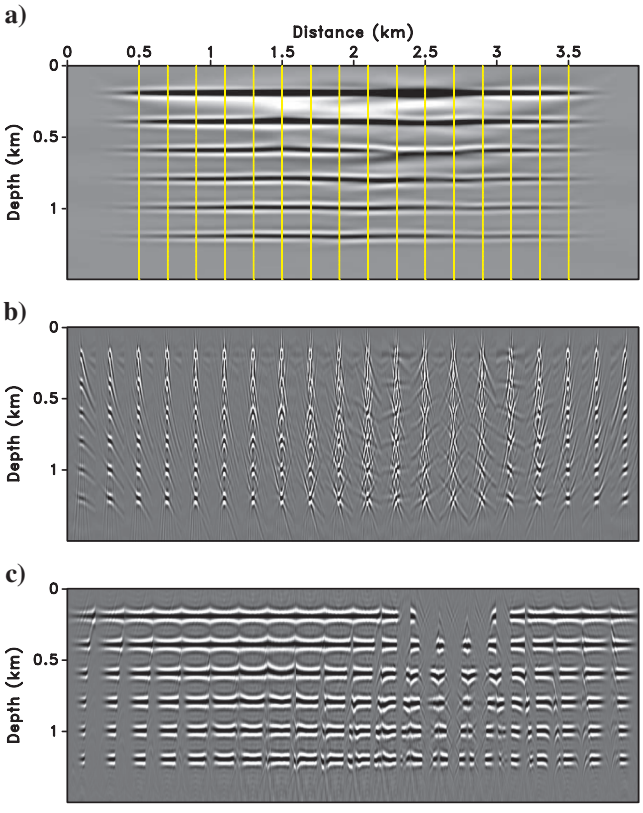


Figure 3. (a) The migrated image, (b) space-lag gathers, and (c) angle-domain gathers obtained using the true model and gap data.

$$\begin{bmatrix} g_s(j,\mathbf{x},\omega) \\ g_r(j,\mathbf{x},\omega) \end{bmatrix} = \begin{bmatrix} \frac{\partial \mathcal{H}'_\lambda}{\partial u_s} \\ \frac{\partial \mathcal{H}'_\lambda}{\partial u_r} \end{bmatrix} = \begin{bmatrix} P_e(\mathbf{x},\boldsymbol{\lambda}) r(\mathbf{x},\boldsymbol{\lambda}) \frac{\partial (P_e(\mathbf{x},\boldsymbol{\lambda}) r(\mathbf{x},\boldsymbol{\lambda}))}{\partial u_s} \\ P_e(\mathbf{x},\boldsymbol{\lambda}) r(\mathbf{x},\boldsymbol{\lambda}) \frac{\partial (P_e(\mathbf{x},\boldsymbol{\lambda}) r(\mathbf{x},\boldsymbol{\lambda}))}{\partial u_r} \end{bmatrix} =$$
$$\begin{bmatrix} P_e(\mathbf{x},\boldsymbol{\lambda}) r(\mathbf{x},\boldsymbol{\lambda}) \left(P_e(\mathbf{x},\boldsymbol{\lambda}) \frac{\partial r(\mathbf{x},\boldsymbol{\lambda})}{\partial u_s} + r(\mathbf{x},\boldsymbol{\lambda}) \frac{\partial P_e(\mathbf{x},\boldsymbol{\lambda})}{\partial u_s} \right) \\ P_e(\mathbf{x},\boldsymbol{\lambda}) r(\mathbf{x},\boldsymbol{\lambda}) \left(P_e(\mathbf{x},\boldsymbol{\lambda}) \frac{\partial r(\mathbf{x},\boldsymbol{\lambda})}{\partial u_r} + r(\mathbf{x},\boldsymbol{\lambda}) \frac{\partial P_e(\mathbf{x},\boldsymbol{\lambda})}{\partial u_r} \right) \end{bmatrix} =$$
$$\begin{bmatrix} \sum_{\boldsymbol{\lambda}} T(\boldsymbol{\lambda}) \{ P_e^2(\boldsymbol{\lambda}) \overline{r(\mathbf{x},\boldsymbol{\lambda})} T(\boldsymbol{\lambda}) u_r(j,\mathbf{x},\omega) - P_e^3(\boldsymbol{\lambda}) \overline{r(\mathbf{x},\boldsymbol{\lambda})} [\mathcal{M}^* \mathcal{M} u_r(j,\mathbf{x},\omega) r'(\mathbf{x})] \} \\ \sum_{\boldsymbol{\lambda}} T(-\boldsymbol{\lambda}) \{ P_e^2(\boldsymbol{\lambda}) r(\mathbf{x},\boldsymbol{\lambda}) T(-\boldsymbol{\lambda}) u_r(j,\mathbf{x},\omega) - P_e^3(\boldsymbol{\lambda}) r(\mathbf{x},\boldsymbol{\lambda}) [\mathcal{M}^* \mathcal{M} u_s(j,\mathbf{x},\omega) r'(\mathbf{x})] \} \end{bmatrix}. \tag{18}$$

Because the adjoint sources computation is the only step associated with the objective function, the rest of the computations are the same as the gradient computation for conventional DSO. Because operator $\mathcal{M}$ has a form similar to $\mathcal{L}$ in equation 2, there is no dependency of $\mathcal{M}$ on either u_s or u_r in equation 18. However, these adjoint sources are expensive to compute because the demigration/migration process is involved in the second term of the adjoint sources.

EXAMPLES

In this section, we use two synthetic examples to illustrate our illumination-compensated image-domain wavefield tomography. In the first example, we use incomplete data to simulate illumination problems due to the acquisition. In the second example, we use the Sigsbee model to test our method in regions of complex geology with poor subsurface illumination caused by irregular salt.

The velocity model for the first example is shown in Figure 1a, and the initial model is the constant background of the true model (Figure 1b). Using six horizontal interfaces as density contrasts, we generate the data at receivers distributed along the surface using a two-way wave-equation finite-difference modeling code. A shot gather is shown in Figure 2. The data are truncated from 2.2 to 2.8 km to simulate an acquisition gap.

To highlight the influence of illumination, we first plot the migrated image and gathers obtained using the gap and full data in the case of the true model. The image and gathers obtained using the gap data and true model are shown in Figure 3, and the image and gathers obtained using the full data and true model are shown in Figure 4. Note that the angle gathers are displayed at selected locations corresponding to the vertical bars overlain in Figures 3a and 4a. It is obvious that illumination due to missing data generates defocusing in space-lag gathers and gaps in angle-domain gathers. Such defocusing is irrelevant to the velocity model error. Next, we plot the migrated image and gathers obtained using the gap and full data in the case of the initial model. The image and gathers obtained using the gap data and initial model are shown in Figure 5, and the image and gathers obtained using the full data and true model are shown in Figure 6. The migrated image for the initial model shows defocusing and crossing events caused by the incorrect model. The space-lag gathers obtained with gap data contain the defocusing due to the illumination and velocity error.

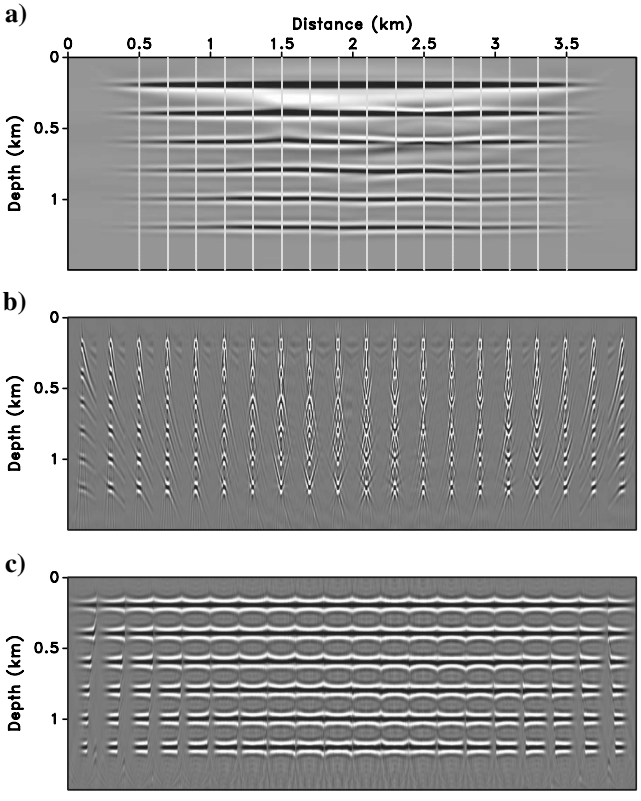


Figure 4. (a) The migrated image, (b) space-lag gathers, and (c) angle-domain gathers obtained using the true model and full data.

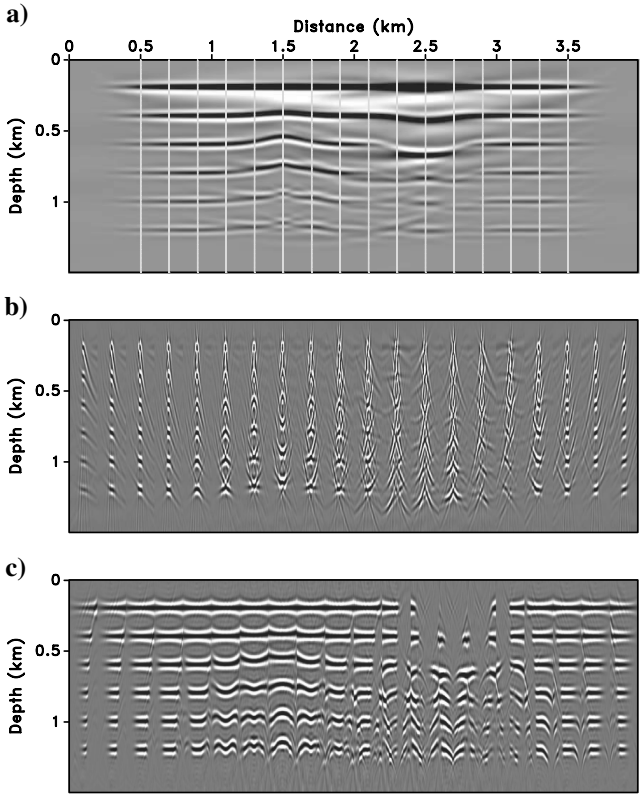


Figure 5. (a) The migrated image, (b) space-lag gathers, and (c) angle-domain gathers obtained using the initial model and gap data.

Downloaded 11/16/13 to 138.67.128.104. Redistribution subject to SEG license or copyright; see Terms of Use at http://library.seg.org/

Downloaded 11/16/13 to 138.67.128.104. Redistribution subject to SEG license or copyright; see Terms of Use at http://library.seg.org/

More importantly, we cannot distinguish between these two different types of defocusing. The illumination gap due to the missing data and the residual moveout caused by the wrong velocity can also be observed in the angle gathers obtained using the gap data.

For comparison with our method, we run the inversion using a conventional DSO penalty operator. Figure 7a plots the penalty operators at the same selected locations shown in Figure 3a. The actual spacing of the gathers and penalty operators is 0.2 km. Because the conventional penalty is laterally invariant, the figure consists of the same operators duplicated at a different lateral position. The inverted model after 30 nonlinear iterations is plotted in Figure 8a, and the corresponding migrated image, space-lag gathers, and angle gathers are shown in Figure 9. The reconstruction of the model is not satisfactory, especially for the anomaly under the acquisition gap. As a result, the reduced quality of the image obtained with the inverted model is not surprising. Although the reflections on the left of the image are quite continuous and flat, those on the right, especially under the acquisition gap, are not flat and are even discontinuous. This result clearly shows the negative impact of the poor illumination on image-domain wavefield tomography.

To show the defocusing due to illumination effects in the gathers, we construct the illumination gathers from the current image. We first pick all the horizons from the image in Figure 5a and replace all the image points on the horizons by point scatterers. The result is the reference image used to generate illumination gathers. We then apply the demigration/migration workflow from equation 15 to the reference image. The result, as shown in Figure 7b, characterizes the illumination effects given the velocity model and acquisition setup.

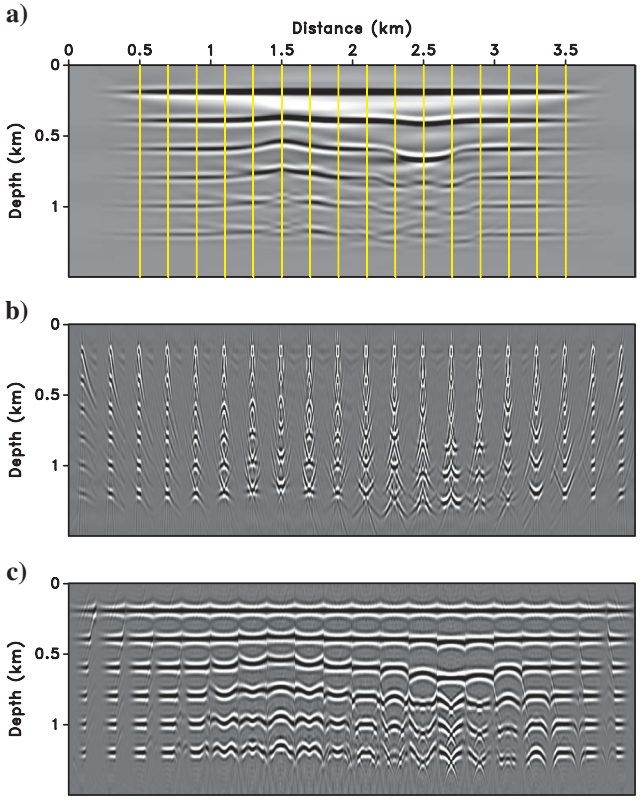


Figure 6. (a) The migrated image, (b) space-lag gathers, and (c) angle-domain gathers obtained using the initial model and full data.

Most reflection energy is focused indicating good illumination, but we can still observe defocusing as the consequence of incomplete data in the area under the acquisition gap. The illumination-based penalty operator is constructed from the gathers in Figure 7b using equation 16, as plotted in Figure 7c. We can observe that the areas in the light color coincide with the focused energy at zero lag and defocusing energy away from zero lag in Figure 7b. Thus, the new operator does not penalize the defocusing due to the uneven illumination and highlights only the defocusing due to velocity errors.

Using the new penalty operator, we update the model under the same conditions as in the example using DSO, Figure 8b. Compared to the result in Figure 8a, the result obtained with the new penalty is cleaner. Also, the anomaly under the acquisition gap is more accurately reconstructed and closer to the true model. The migrated image, space-lag gathers, and angle-domain gathers are shown in Figure 10. Because of the improved model, the images are also improved, as seen in Figure 10a. The reflections under the acquisition gap are more continuous and flat than the image in Figure 9a. In addition, one can observe from the angle gathers in Figure 9c that more events appear in the area under the acquisition gap and overall reflections are flatter, which indicates an improved signal-to-noise ratio rising from the more accurate reconstructed model.

We also apply our method to the Sigsbee 2A model (Paffenholz et al., 2002), and we concentrate on the subsalt region. The target area ranges from $x = 6.5$ to 20 km and from $z = 4.5$ to 9 km. The true and initial models are shown in Figure 11a and 11b. Here, we

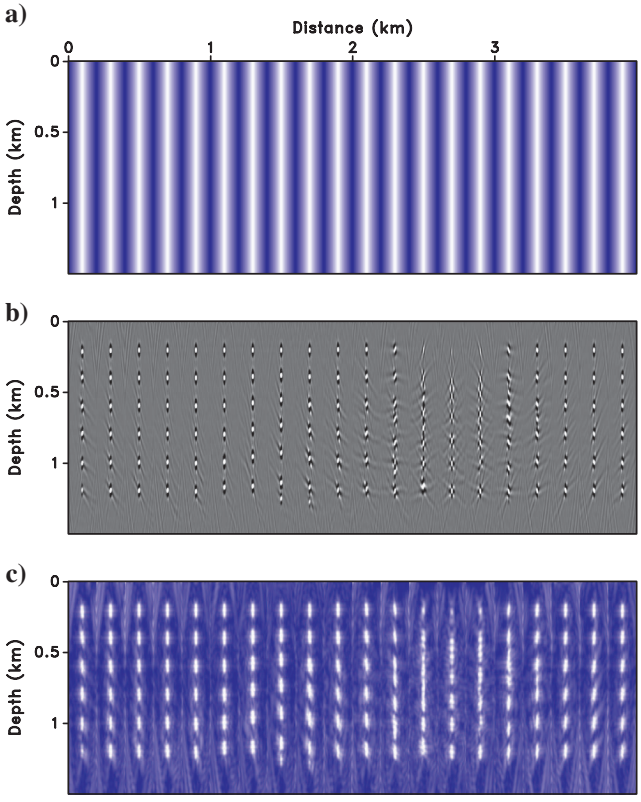


Figure 7. (a) The conventional DSO penalty operator. (b) The gathers obtained with demigration/migration showing the illumination effects. (c) The illumination-based penalty operator constructed from the gathers in (b). The light areas cover the defocusing due to the illumination.

switch to show velocity instead of slowness to better visualize the model. The migrated image, space-lag gathers, and angle-domain gathers for correct and initial models are shown in Figures 12 and 13, respectively. The angle gathers are displayed at selected locations corresponding to the vertical bars overlain in Figures 12a and 13a. The actual spacing of the gathers and penalty operators is 0.45 km. Note that the reflections in the angle gathers appear only at positive angles because the data are simulated for towed streamers and the subsurface is illuminated from one side only. Just as for the previous example, we run the inversion using the conventional DSO

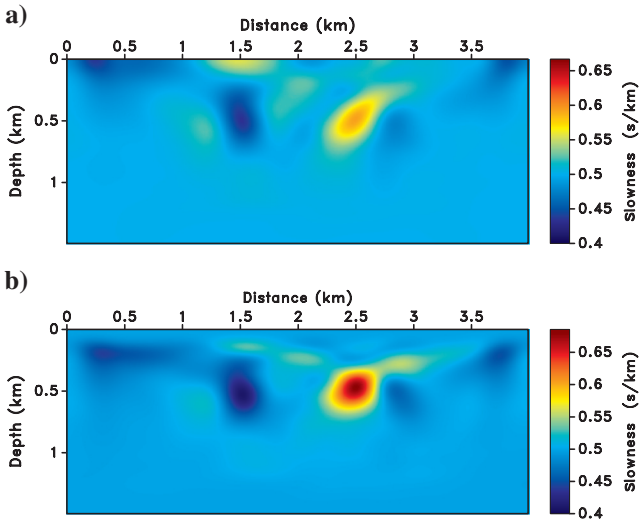


Figure 8. The reconstructed models using (a) the conventional DSO penalty and (b) the illumination-based penalty.

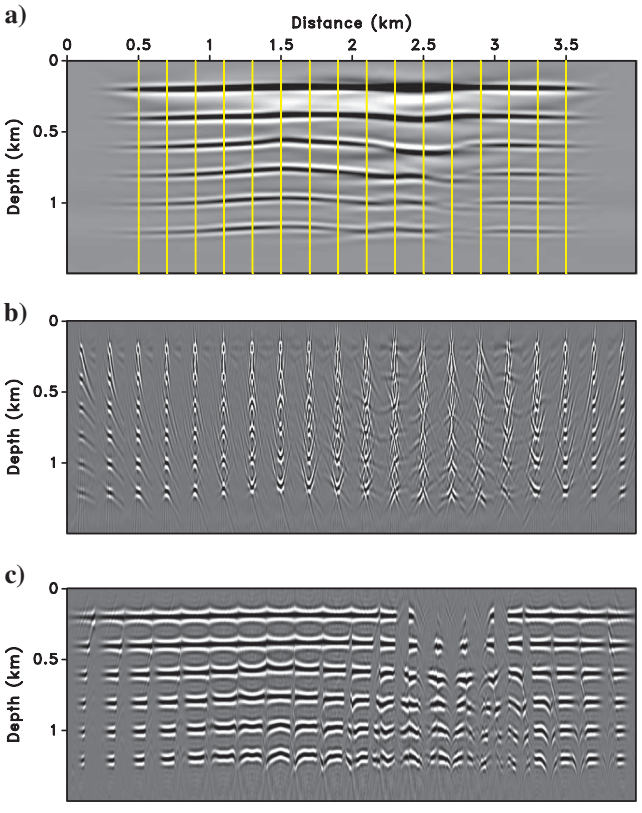


Figure 9. (a) The migrated image, (b) space-lag gathers, and (c) angle-domain gathers obtained using the reconstructed model with the DSO penalty.

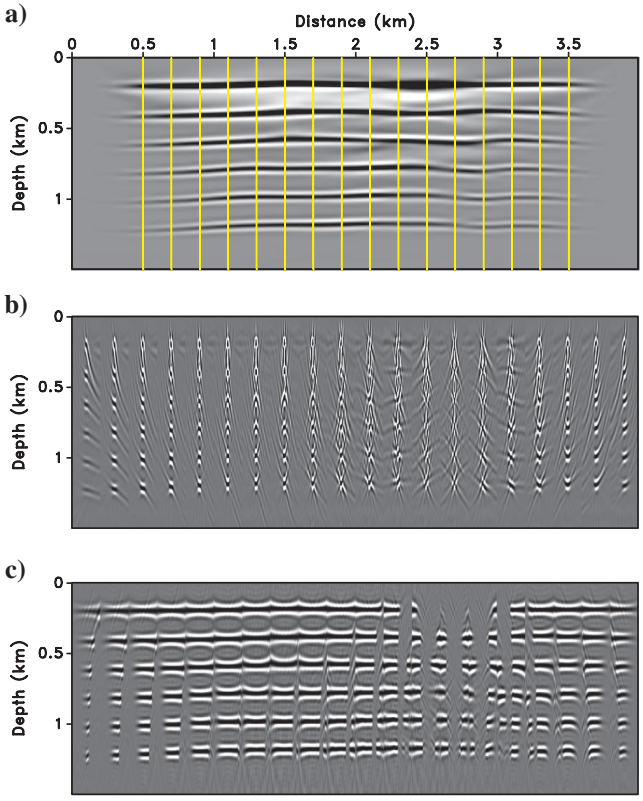


Figure 10. (a) The migrated image, (b) space-lag gathers, and (c) angle-domain gathers obtained using the reconstructed model with the illumination-based penalty.

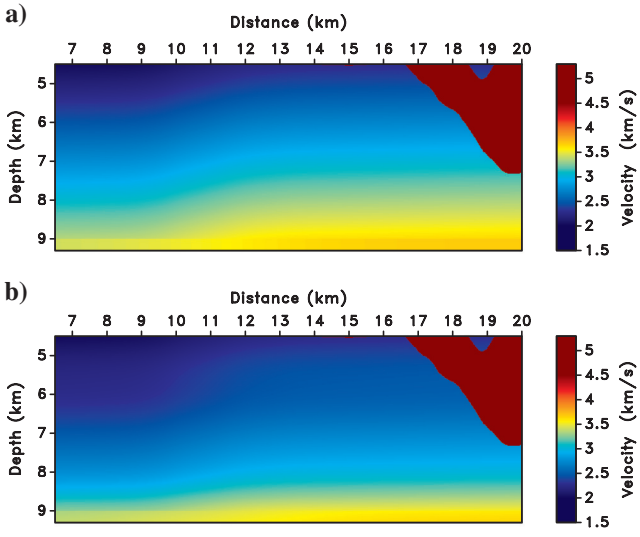


Figure 11. (a) The true model and (b) the initial model in the target area of the Sigsbee model.

Downloaded 11/16/13 to 138.67.128.104. Redistribution subject to SEG license or copyright; see Terms of Use at http://library.seg.org/

Downloaded 11/16/13 to 138.67.128.104. Redistribution subject to SEG license or copyright; see Terms of Use at http://library.seg.org/

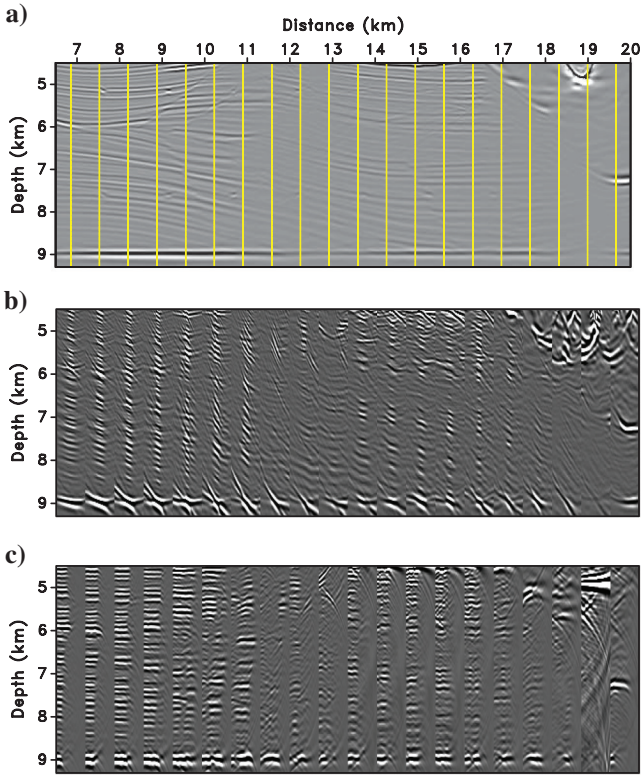


Figure 12. (a) The migrated image, (b) space-lag gathers, and (c) the angle-domain gathers obtained using the true model.

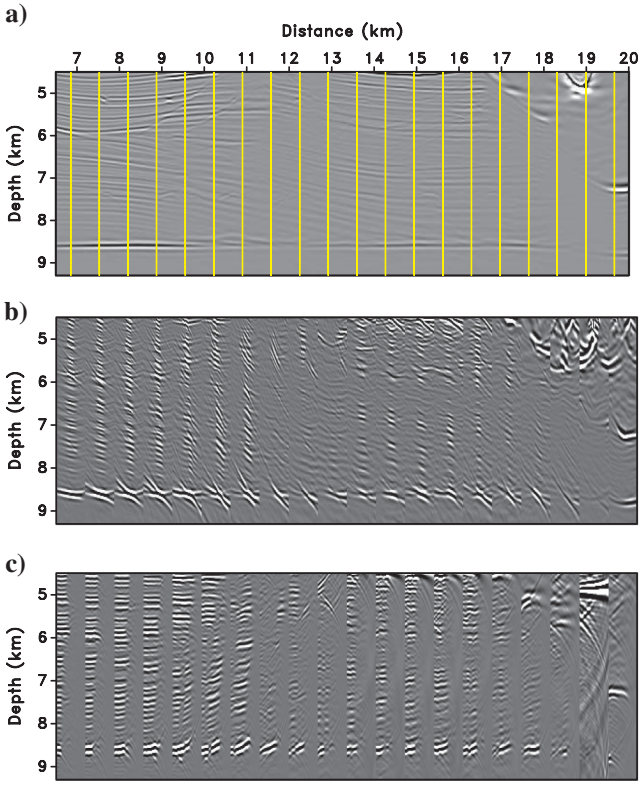


Figure 13. (a) The migrated image, (b) space-lag gathers, and (c) the angle-domain gathers obtained using the initial model.

penalty and the illumination-based penalty operators. For the illumination-based operator, we first generate gathers containing defocusing due to illumination (Figure 14a), and then we construct the penalty operator as shown in Figure 14b using equation 16. From the gathers characterizing the illumination effects, we can observe the significant defocusing in the subsalt area because the salt distorts the wavefields used for imaging and causes the poor illumination in this area.

We run both inversions for 20 iterations, and we obtain the reconstructed models shown in Figure 15. The corresponding migrated image, space-lag gathers, and angle-domain gathers shown in Figures 16 and 17, respectively. The model obtained using

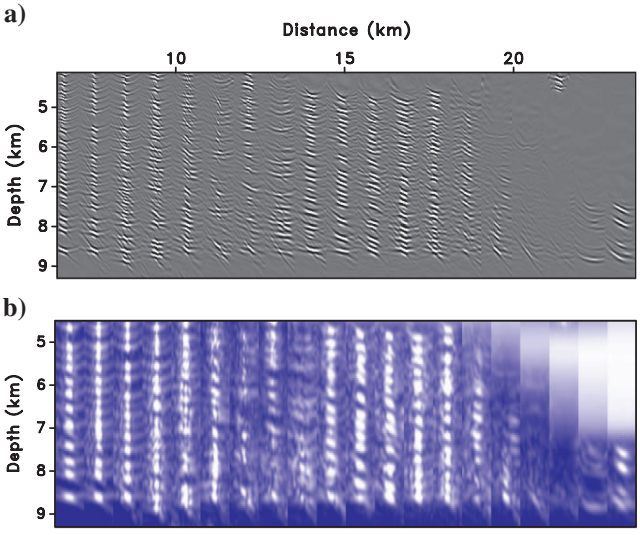


Figure 14. (a) The gathers obtained with demigration/migration showing the illumination effects. (b) The illumination-based penalty operator constructed from the gathers in (a). The light areas cover the defocusing due to the illumination.

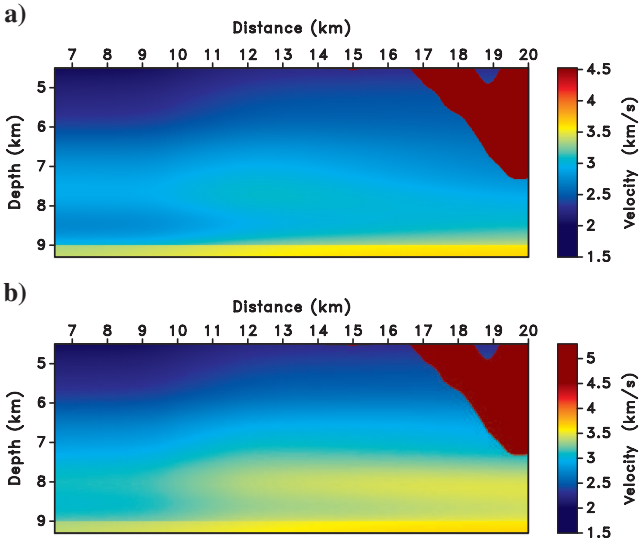


Figure 15. The reconstructed models using (a) the DSO penalty and (b) the illumination-based penalty.

Downloaded 11/16/13 to 138.67.128.104. Redistribution subject to SEG license or copyright; see Terms of Use at http://library.seg.org/

the illumination-based penalty is much closer to the true model than the model obtained using the DSO penalty. The DSO model is not sufficiently updated and is too slow. This is because the severe defocusing due to the salt biases the inversion when we do not take into accounts the uneven illumination for tomography. The comparison of the images also suggests that the inversion using the illumination-based penalty is superior to the inversion using the DSO penalty. The image obtained with the new penalty is significantly improved, as illustrated, for example, by the fact that the diffractors distributed at $z = 7.6$ km focus and the faults located between $x = 14.0$ km, $z = 6.0$ km and $x = 16.0$ km, $z = 9.0$ km are more visible in the images. If we concentrate on the bottom reflector (around 9 km), we can see that the bottom reflector is corrected to the right depth for inversion using the illumination-based penalty, whereas the bottom reflector for inversion using the DSO penalty is still away from the right depth and not as flat as the reflector in Figure 17a. From the angle gathers obtained using different models, we can see that the gathers for both reconstructed models show flatter reflections, indicating that the reconstructed models are more accurate than the initial model. We can, nonetheless, observe that the reflections in Figure 17c are flatter than those in Figure 16c, and we conclude that the reconstructed model using the illumination-based penalty is more accurate.

DISCUSSION

Uneven illumination is a challenge often faced by exploration activities in complex subsurface environments, particularly in subsalt areas. Furthermore, imperfect acquisition can also cause illumination problems. In either case, the reflections from various angles cannot be observed on the surface, either because of the complexity of the subsurface or because of limited/partial acquisition on the surface. The more essential reason of the illumination problem, however, is due to the nonunitary nature of the migration operator. One can also use an improved migration operator to compensate the illumination problem, as Tang and Biondi (2011) suggest. In any of these situations, the effectiveness of image-domain wavefield tomography deteriorates. In comparison, data-domain wavefield tomography methods suffer less from the illumination. However, the image-domain approach is more effective for extracting velocity model information from reflections than the data-domain approach in a deeper target such as subsalt. To make the image-domain method more applicable in practice, we must compensate the illumination effects to improve its accuracy. From the synthetic example, we see that the imbalanced illumination creates defocusing in space-lag gathers regardless of the accuracy of the velocity model. Minimizing such defocusing through wavefield tomography generates incorrect updates and artifacts in the result. Therefore, the defocusing caused by the uneven illumination must be excluded from the model building process. This is done by replacing the DSO penalty operator with a modified penalty operator, which is constructed based on the illumination information. One might also implement a similar idea for DSO formulated in the angle domain because uneven illumination appears as a hole and velocity error generates residual moveout. However, the transformation to the angle domain brings additional computational cost. Shen and Symes (2008) also

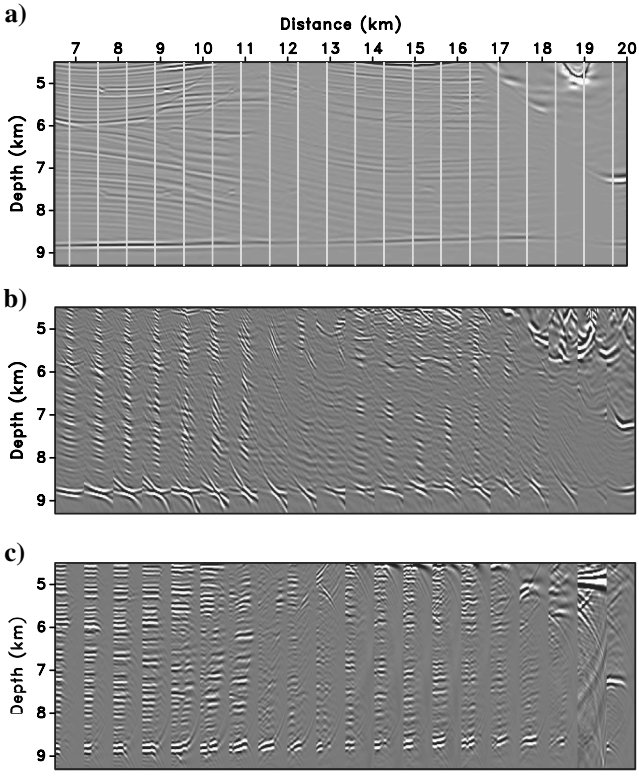


Figure 16. (a) The migrated image, (b) space-lag gathers, and (c) the angle-domain gathers obtained using the model reconstructed with the DSO penalty.

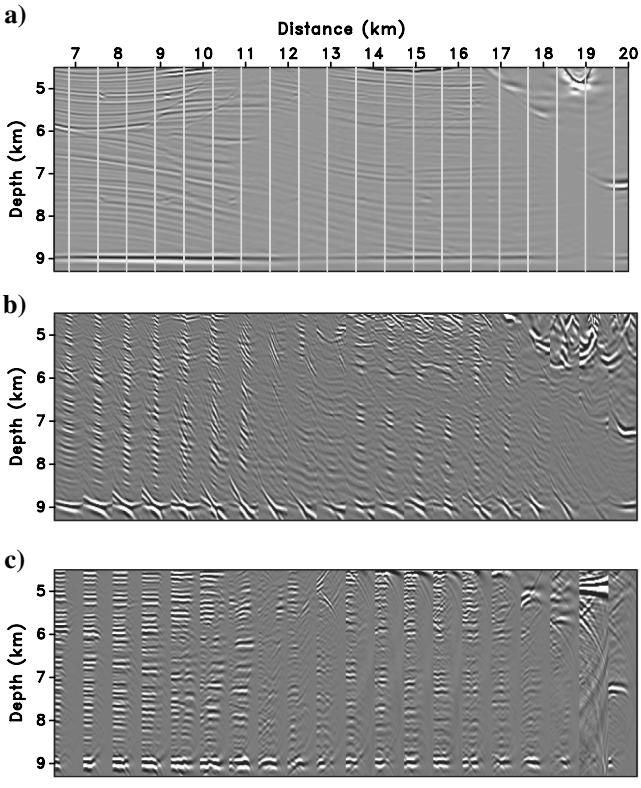


Figure 17. (a) The migrated image, (b) space-lag gathers, and (c) the angle-domain gathers obtained using the model reconstructed with the illumination-based penalty.

Downloaded 11/16/13 to 138.67.128.104. Redistribution subject to SEG license or copyright; see Terms of Use at http://library.seg.org/

observe that the results obtained in the angle domain are worse than the results obtained in the lag domain because of the larger condition number of the system. Thus, we only present the approach implemented based on the space-lag gathers. During our iterative inversion, we update the penalty operator at each iteration because the velocity model is changing during the iterations and the subsurface illumination information needs to be reevaluated.

In the theory section, we discussed the formulation of image-domain wavefield tomography and our solution to illumination problems based on a two-way wave equation. The formulation, however, applies well when a one-way wave equation is used. The construction of the illumination-based penalty operator is similar, except for the wave equation used in all modeling and migrations.

CONCLUSIONS

We have demonstrated an illumination compensation strategy for wavefield tomography in the image domain. The idea is to measure the illumination effects on space-lag extended images, and replace the conventional DSO penalty operator with a new one that compensates for illumination. This approach isolates the defocusing caused by the illumination such that the inversion minimizes only the defocusing relevant to the velocity error. Synthetic examples demonstrate the negative effects of uneven illumination on the reconstructed model and show the improvements on the inversion results and migrated images after the illumination information is included in the penalty operator. Our approach enhances the robustness and effectiveness of image-domain wavefield tomography when the surface data are incomplete or when the subsurface illumination is uneven due to complex geologic structures such as salt.

ACKNOWLEDGMENTS

We acknowledge the support of the sponsors of the Center for Wave Phenomena at the Colorado School of Mines. The reproducible numeric examples in this paper use the Madagascar open-source software package freely available from http://www.ahay.org. This research was supported in part by the Golden Energy Computing Organization at the Colorado School of Mines using resources acquired with financial assistance from the National Science Foundation and the National Renewable Energy Laboratory.

REFERENCES

Al-Yahya, K., 1989, Velocity analysis by iterative profile migration: Geophysics, **54**, 718–729, doi: 10.1190/1.1442699.

Berkhout, A., 1982, Seismic migration: Imaging of acoustic energy by wavefield extrapolation. Part A: Theoretical aspects, 2nd ed.: Elsevier Science.

Biondi, B., and W. Symes, 2004, Angle-domain common-image gathers for migration velocity analysis by wavefield-continuation imaging: Geophysics, **69**, 1283–1298, doi: 10.1190/1.1801945.

Etgen, J., S. H. Gray, and Y. Zhang, 2009, An overview of depth imaging in exploration geophysics: Geophysics, **74**, no. 6, WCA5–WCA17, doi: 10.1190/1.3223188.

Gherasim, M., U. Albertin, B. Nolte, and O. Askim, 2010, Wave-equation angle-based illumination weighting for optimized subsalt imaging: 80th Annual International Meeting, SEG, Expanded Abstracts, 3293–3297.

Gray, S. H., J. Etgen, J. Dellinger, and D. Whitmore, 2001, Seismic migration problems and solutions: Geophysics, **66**, 1622–1640, doi: 10.1190/1.1487107.

Guitton, A., 2004, Amplitude and kinematic corrections of migrated images for nonunitary imaging operators: Geophysics, **69**, 1017–1024, doi: 10.1190/1.1778244.

Knyazev, A. V., and I. Lashuk, 2007, Steepest descent and conjugate gradient methods with variable preconditioning: SIAM Journal on Matrix Analysis and Applications, **29**, 1267–1280, doi: 10.1137/060675290.

Leveille, J. P., I. F. Jones, Z. Z. Zhou, B. Wang, and F. Liu, 2011, Subsalt imaging for exploration, production, and development: A review: Geophysics, **76**, no. 5, WB3–WB20, doi: 10.1190/geo2011-0156.1.

Mao, J., R. S. Wu, and J. H. Gao, 2010, Directional illumination analysis using the local exponential frame: Geophysics, **75**, no. 4, S163–S174, doi: 10.1190/1.3454361.

Nemeth, T., C. Wu, and G. T. Schuster, 1999, Least-square migration of incomplete reflection data: Geophysics, **64**, 208–221, doi: 10.1190/1.1444517.

Paffenholz, J., B. McLain, J. Zaske, and P. Keliher, 2002, Subsalt multiple attenuation and imaging: Observations from the Sigsbee 2B synthetic dataset: 72nd Annual International Meeting, SEG, Expanded Abstracts, 2122–2125.

Plessix, R.-E., 2006, A review of the adjoint state method for computing the gradient of a functional with geophysical applications: Geophysical Journal International, **167**, 495–503, doi: 10.1111/j.1365-246X.2006.02978.x.

Plessix, R.-E., 2009, Three-dimensional frequency-domain full-waveform inversion with an iterative solver: Geophysics, **74**, no. 6, WCC149–WCC157, doi: 10.1190/1.3211198.

Pratt, R. G., 1999, Seismic waveform inversion in the frequency domain, Part 1: Theory and verification in a physical scale model: Geophysics, **64**, 888–901, doi: 10.1190/1.1444597.

Rickett, J., and P. Sava, 2002, Offset and angle-domain common image-point gathers for shot-profile migration: Geophysics, **67**, 883–889, doi: 10.1190/1.1484531.

Sava, P., and B. Biondi, 2004a, Wave-equation migration velocity analysis — I: Theory: Geophysical Prospecting, **52**, 593–606, doi: 10.1111/j.1365-2478.2004.00447.x.

Sava, P., and B. Biondi, 2004b, Wave-equation migration velocity analysis — II: Subsalt imaging examples: Geophysical Prospecting, **52**, 607–623, doi: 10.1111/j.1365-2478.2004.00448.x.

Sava, P., and S. Fomel, 2003, Angle-domain common image gathers by wavefield continuation methods: Geophysics, **68**, 1065–1074, doi: 10.1190/1.1581078.

Shen, P., and H. Calandra, 2005, One-way waveform inversion within the framework of adjoint state differential migration: 75th Annual International Meeting, SEG, Expanded Abstracts, 1709–1712.

Shen, H., S. Mothi, and U. Albertin, 2011, Improving subsalt imaging with illumination-based weighting of RTM 3D angle gathers: 81st Annual International Meeting, SEG, Expanded Abstracts, 3206–3211.

Shen, P., C. Stolk, and W. Symes, 2003, Automatic velocity analysis by differential semblance optimization: 73rd Annual International Meeting, SEG, Expanded Abstracts, 2132–2135.

Shen, P., and W. W. Symes, 2008, Automatic velocity analysis via shot profile migration: Geophysics, **73**, no. 5, VE49–VE59, doi: 10.1190/1.2972021.

Sirgue, L., and R. Pratt, 2004, Efficient waveform inversion and imaging: A strategy for selecting temporal frequencies: Geophysics, **69**, 231–248, doi: 10.1190/1.1649391.

Stolk, C. C., and W. W. Symes, 2004, Kinematic artifacts in prestack depth migration: Geophysics, **69**, 562–575, doi: 10.1190/1.1707076.

Stork, C., 1992, Reflection tomography in the postmigrated domain: Geophysics, **57**, 680–692, doi: 10.1190/1.1443282.

Symes, W., 2008a, Approximate linearized inversion by optimal scaling of prestack depth migration: Geophysics, **73**, no. 2, R23–R35, doi: 10.1190/1.2836323.

Symes, W., 2008b, Migration velocity analysis and waveform inversion: Geophysical Prospecting, **56**, 765–790, doi: 10.1111/j.1365-2478.2008.00698.x.

Symes, W. W., and J. J. Carazzone, 1991, Velocity inversion by differential semblance optimization: Geophysics, **56**, 654–663, doi: 10.1190/1.1443082.

Tang, Y., and B. Biondi, 2011, Target-oriented wavefield tomography using synthesized born data: Geophysics, **76**, no. 5, WB191–WB207, doi: 10.1190/geo2010-0383.1.

Tarantola, A., 1984, Inversion of seismic reflection data in the acoustic approximation: Geophysics, **49**, 1259–1266, doi: 10.1190/1.1441754.

Vigh, D., and E. W. Starr, 2008, 3D prestack plane-wave, full-waveform inversion: Geophysics, **73**, no. 5, VE135–VE144, doi: 10.1190/1.2952623.

Virieux, J., and S. Operto, 2009, An overview of full-waveform inversion in exploration geophysics: Geophysics, **74**, no. 6, WCC1–WCC26, doi: 10.1190/1.3238367.

Woodward, M., D. Nichols, O. Zdraveva, P. Whitfield, and T. Johns, 2008, A decade of tomography: Geophysics, **73**, no. 5, VE5–VE11, doi: 10.1190/1.2969907.

Woodward, M. J., 1992, Wave-equation tomography: Geophysics, **57**, 15–26, doi: 10.1190/1.1443179.

Xie, X. B., S. Jin, and R. S. Wu, 2006, Wave-equation-based seismic illumination analysis: Geophysics, **71**, no. 5, S169–S177, doi: 10.1190/1.2227619.

Yang, T., and P. Sava, 2010, Moveout analysis of wave-equation extended images: Geophysics, **75**, no. 4, S151–S161, doi: 10.1190/1.3460296.

Yu, J., and T. Schuster, 2003, Migration deconvolution vs. least squares migration: 74th Annual International Meeting, SEG, Expanded Abstracts, 1047–1050.

Zhang, S., and G. Schuster, 2010, Wave-equation reflection traveltime inversion: 80th Annual International Meeting, SEG, Expanded Abstracts, 2705–2710.

Downloaded 11/16/13 to 138.67.128.104. Redistribution subject to SEG license or copyright; see Terms of Use at http://library.seg.org/